

Supporting Information

for

Dielectric Properties of Zeolitic Imidazolate Frameworks in the Broadband Infrared Regime

**Matthew R. Ryder,^{1,2,3} Zhixin Zeng,¹ Kirill Titov,¹ Yueting Sun,¹ E.M. Mahdi,¹ Irina Flyagina,¹
Thomas D. Bennett,⁴ Bartolomeo Civalleri,⁵ Chris S. Kelley,² Mark D. Frogley,²
Gianfelice Cinque,² and Jin-Chong Tan^{1*}**

¹*Multifunctional Materials & Composites (MMC) Laboratory, Department of Engineering Science,
University of Oxford, Parks Road, Oxford OX1 3PJ, United Kingdom*

²*Diamond Light Source, Harwell Campus, Chilton, Oxford OX11 0DE, United Kingdom*

³*ISIS Facility, Rutherford Appleton Laboratory, Chilton, Didcot OX11 0QX, United Kingdom*

⁴*Department of Materials Science and Metallurgy, University of Cambridge,
Cambridge CB3 0FS, United Kingdom*

⁵*Department of Chemistry, NIS and INSTM Reference Centre, University of Turin,
via Pietro Giuria 7, 10125 Torino, Italy*

*Correspondence to: jin-chong.tan@eng.ox.ac.uk

Table of Contents

1	Materials Synthesis and Characterization.....	3
2	Experimental Setup and Analysis of Reflectivity Data	9
3	Pellet Surface Characterization	11
4	Reflectivity Spectra in the Far-IR and Mid-IR Regions	14
5	Real and Imaginary Parts of the Complex Dielectric Constant and Complex Refractive Index.....	15
6	<i>Ab Initio</i> Density Functional Theory (DFT) Calculations	19
7	ZIF-8 Spectral Features and Correction	22
8	References.....	23

1 Materials Synthesis and Characterization

The ZIF samples were obtained from the following methods:

- ZIF-4 – Synthesized according to ref.1, the same sample batch as per ref.2
- ZIF-7 – Synthesized according to ref.3 (reaction time was 24h instead of 48h).
- ZIF-8 – Purchased from Sigma-Aldrich, Basolite[®] Z1200.
- ZIF-71 – Synthesized according to ref.4 (zinc acetate dihydrate was used instead of zinc acetate and chloroform was not used).
- ZIF-90 – Synthesized according to ref.5

Before the infrared reflectivity experiments, the purity and crystallinity of the powdered samples were confirmed using powder X-ray diffraction (PXRD).

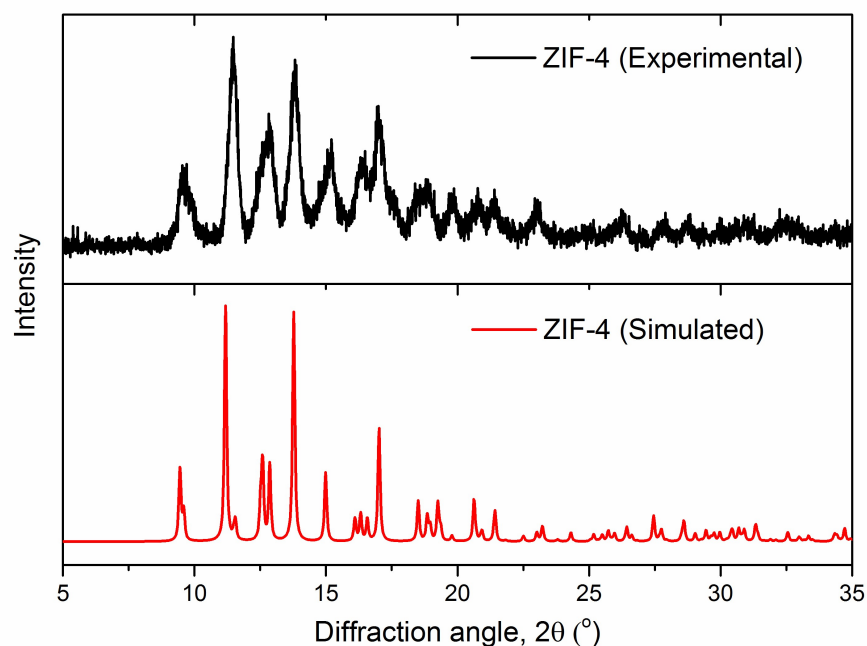


Fig. S1. PXRD of ZIF-4 comparing the experimental spectrum for the sample used in the measurements and the simulated spectrum from the CIF file (CCDC code: VEJYUF)⁶ in the literature.

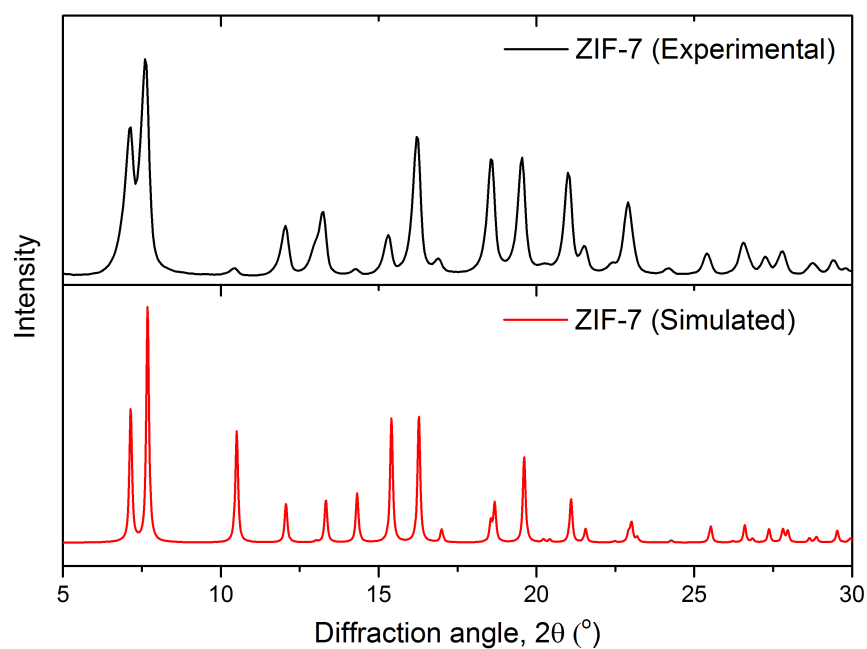


Fig. S2. PXRd of ZIF-7 (phase-I) comparing the experimental spectrum for the sample used in the measurements and the simulated spectrum from the CIF file (CCDC code: VELVIS)⁶ in the literature.

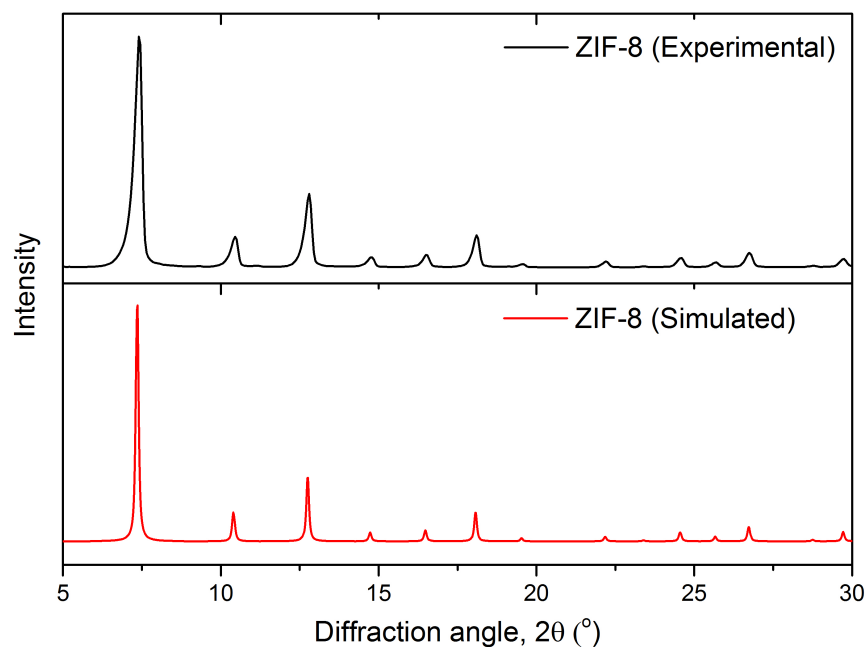


Fig. S3. PXRd of ZIF-8 comparing the experimental spectrum for the sample used in the measurements and the simulated spectrum from the CIF file (CCDC code: VELVOY)⁶ in the literature.

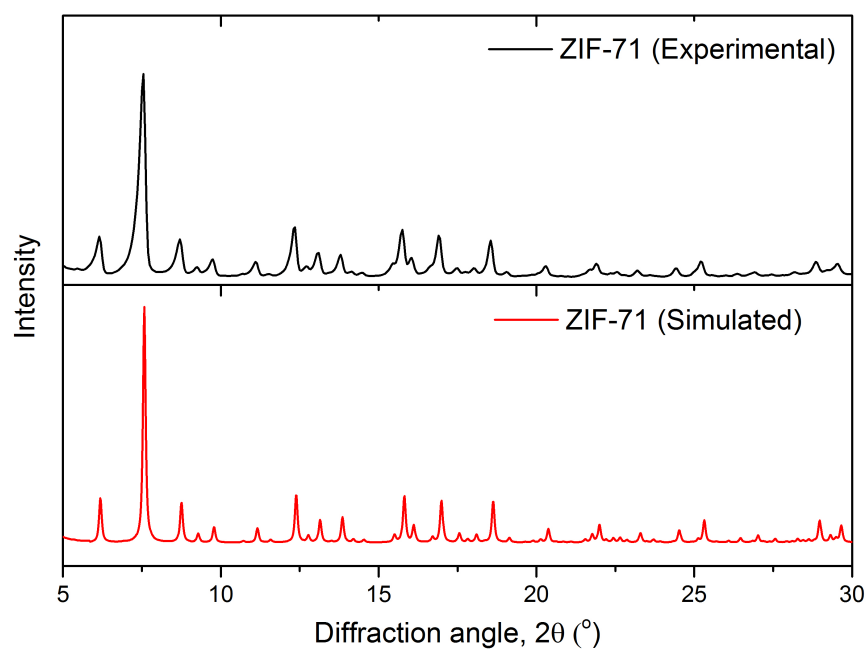


Fig. S4. PXRd of ZIF-71 comparing the experimental spectrum for the sample used in the measurements and the simulated spectrum from the CIF file (CCDC code: GITVIP)⁶ in the literature.

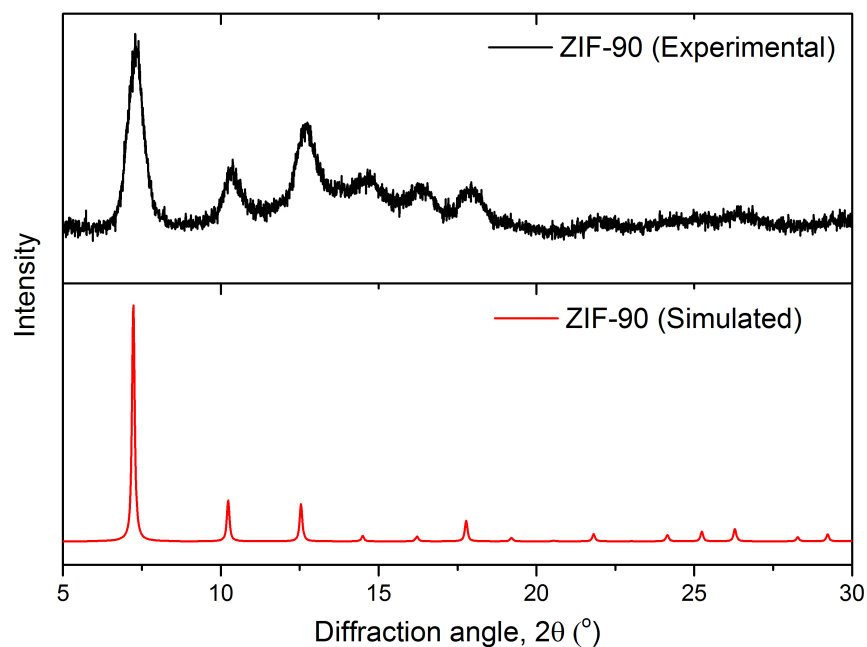


Fig. S5. PXRd of ZIF-90 comparing the experimental spectrum for the sample used in the measurements and the simulated spectrum from the CIF file (CCDC code: WOJGEI)⁶ in the literature. The Bragg peak broadening is due to its fine nanocrystal size of ~100 nm.

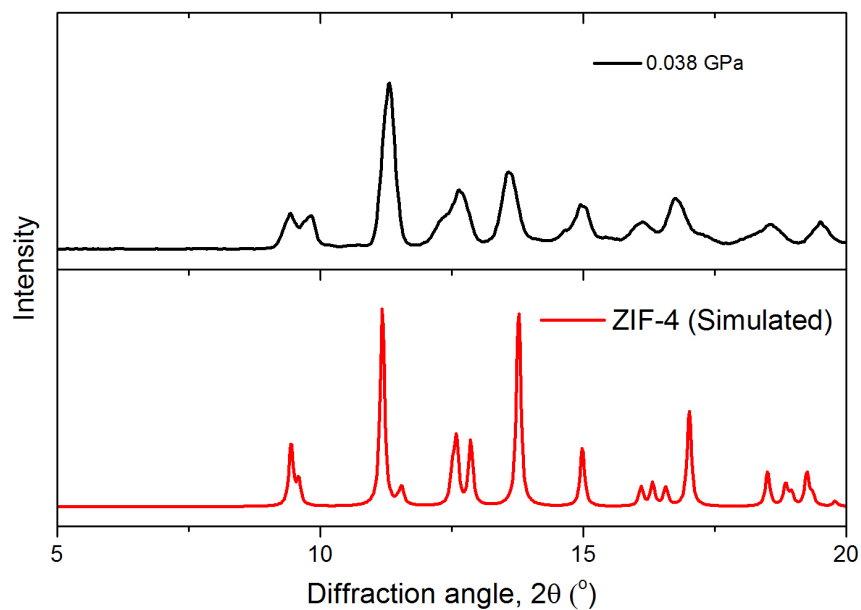


Fig. S6. PXRd of the ZIF-4 pellet compared with the simulated spectrum from the CIF file in the literature (CCDC code: VEJYUF).⁶

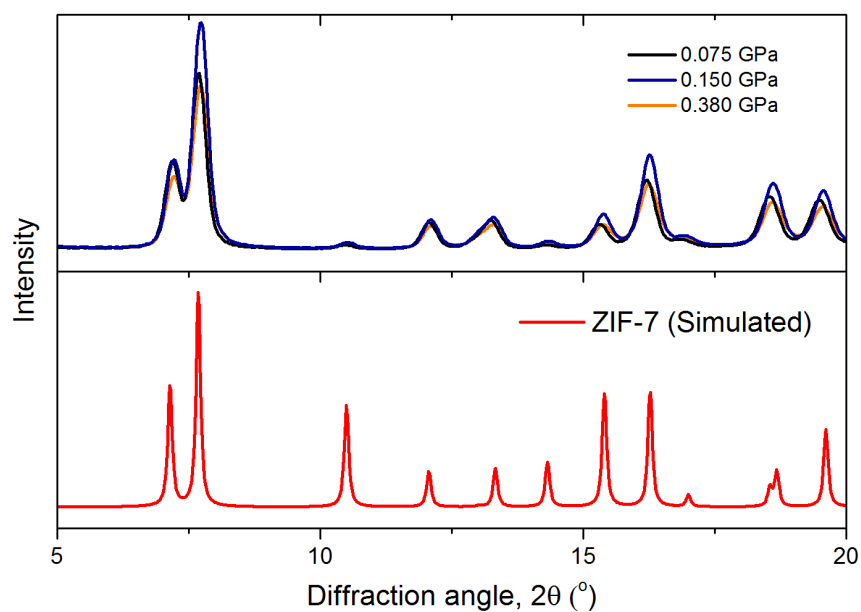


Fig. S7. PXRd of the ZIF-7 (phase I) pellets at the varying pelletization pressures compared with the simulated spectrum from the CIF file in the literature (CCDC code: VELVIS).⁶ The spectra show remarkable resilience to pelletization pressure. The mechanical stability may be attributed to the occluded solvent molecules occupying the pores of the phase-I of ZIF-7.⁷

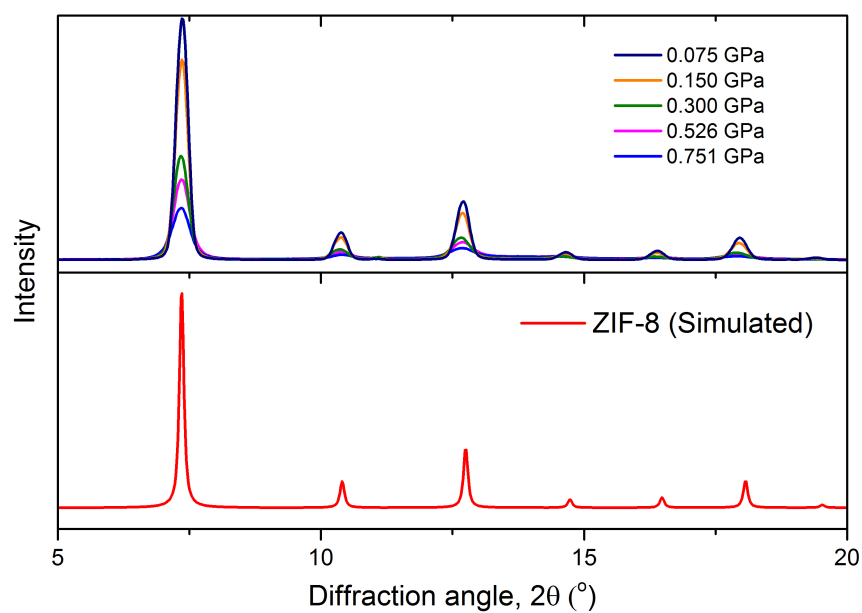


Fig. S8. PXR D of the ZIF-8 pellets at the varying pelletization pressures compared with the simulated spectrum from the CIF file in the literature (CCDC code: VELVOY).⁶ The spectra clearly show the loss of Bragg intensity with increasing pelletization pressure.

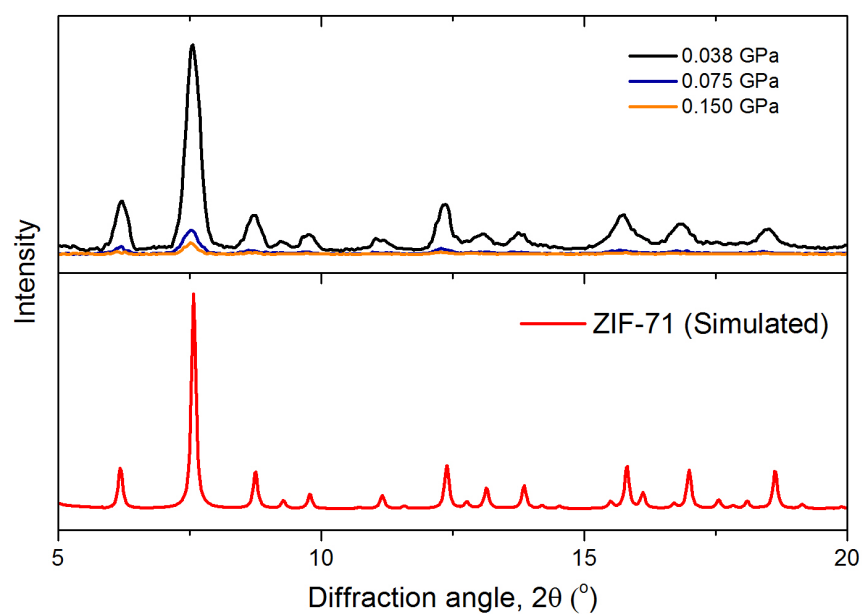


Fig. S9. PXR D of the ZIF-71 pellets at the varying pelletization pressures compared with the simulated spectrum from the CIF file in the literature (CCDC code: GITVIP).⁶ The spectra show the loss of Bragg intensity with increasing pelletization pressure.

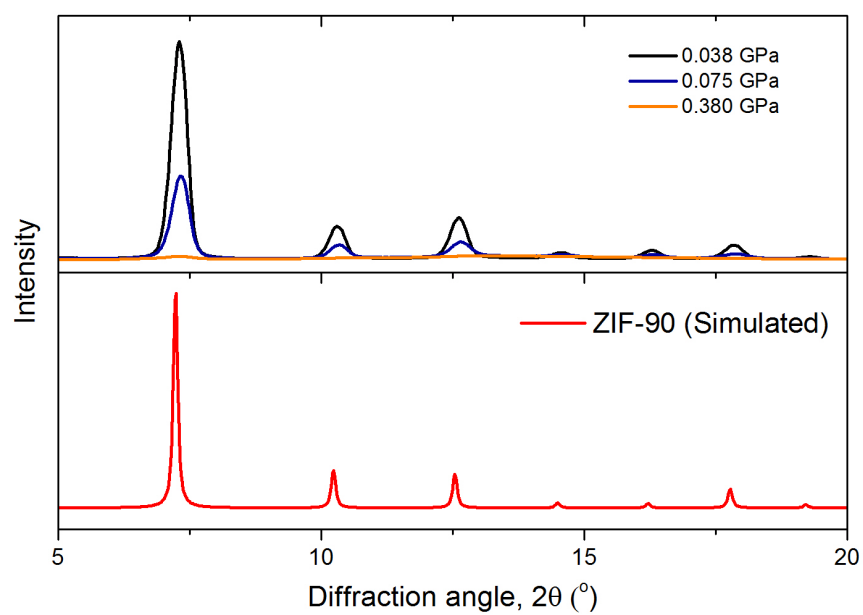


Fig. S10. PXRD of the ZIF-90 pellets at the varying pelletization pressures compared with the simulated spectrum from the CIF file in the literature (CCDC code: WOJGEI).⁶ The spectra clearly show the loss of Bragg intensity with pelletization pressure.

2 Experimental Setup and Analysis of Reflectivity Data

The IR spectroscopy experiments were performed at Beamline B22 MIRIAM in the Diamond Light Source synchrotron. Specular reflection measurements were carried out under vacuum *via* a Bruker Vertex 80V Fourier Transform IR (FTIR) interferometer equipped with the Pike Technologies VeeMAX II variable angle specular reflectance accessories.⁸ IR reflectivity spectra were collected on samples of pressed powder pellets (diameter = 13 mm, thickness ~1 mm), prepared using uniaxial compression varied from 0.1-10 tons. The reflectivity spectra were obtained at an angle of incidence of 30° from the vertical axis.

The measurements were obtained at a resolution of 4 cm⁻¹ with a 6-μm thick Mylar broadband multi-layer coated beam splitter to allow for measurements to be obtained in the spectral range below 700 cm⁻¹. For the mid-IR (MIR) spectra, a KBr beam splitter was used to measure the spectral range from 500-9000 cm⁻¹. The signal-to-noise of far-IR spectra reported was significantly increased due to the utilisation of an IR Labs liquid helium cooled Si bolometer.

Far-IR Data Acquisition Parameters	
Scanner Velocity	120 kHz
Spectral Resolution	4 cm ⁻¹
Phase Resolution	32 cm ⁻¹

Mid-IR Data Acquisition Parameters	
Scanner Velocity	40 kHz
Spectral Resolution	2 cm ⁻¹
Phase Resolution	32 cm ⁻¹

Kramers-Kronig Transformations (KKT)⁹ were performed to calculate the complex dielectric function and complex refractive index from the reflectivity spectra implemented in the Bruker OPUS software.¹⁰ The real and imaginary parts of the complex refractive index $\tilde{n}(\omega) = n(\omega) + i\kappa(\omega)$, the complex dielectric constant $\tilde{\epsilon}(\omega) = \epsilon'(\omega) + i\epsilon''(\omega)$, and the logarithm of

the amplitude-reflectivity $\ln(re^{i\phi}) = \ln(r) + i\phi$, are dependent on each other because of the causality principle. The two parts can be transformed into each other *via* KKT.⁹ First, the OPUS spectroscopy software¹⁰ uses KKT to calculate the phase rotation angle $\phi(\omega)$ [as a function of frequency ω] from the measured reflectance spectrum $R(\omega) = r^2(\omega)$ of an optically thick sample. Then the reflectivity of the air/sample edge (vertical incidence) is calculated from $r(\omega)$ and $\phi(\omega)$ using the Fresnel equation:

$$\Gamma(\omega)e^{i\phi(\omega)} = \frac{n(\omega) - 1}{n(\omega) + 1}$$

The real and imaginary parts of the complex refractive index, $\tilde{n}(\omega)$, can then be calculated as follows:

$$n(\omega) = \frac{1 - R(\omega)}{1 + R(\omega) - R^{\frac{1}{2}}(\omega) \cos(\phi(\omega))}$$

$$\kappa(\omega) = \frac{2R^{\frac{1}{2}}(\omega) \sin(\phi(\omega))}{1 + R(\omega) - R^{\frac{1}{2}}(\omega) \cos(\phi(\omega))}$$

Finally, the real and imaginary parts of the complex dielectric function, $\tilde{\epsilon}(\omega)$, can be determined using the following relations:

$$\epsilon'(\omega) = n(\omega)^2 - \kappa(\omega)^2$$

$$\epsilon''(\omega) = 2n(\omega)\kappa(\omega)$$

3 Pellet Surface Characterization

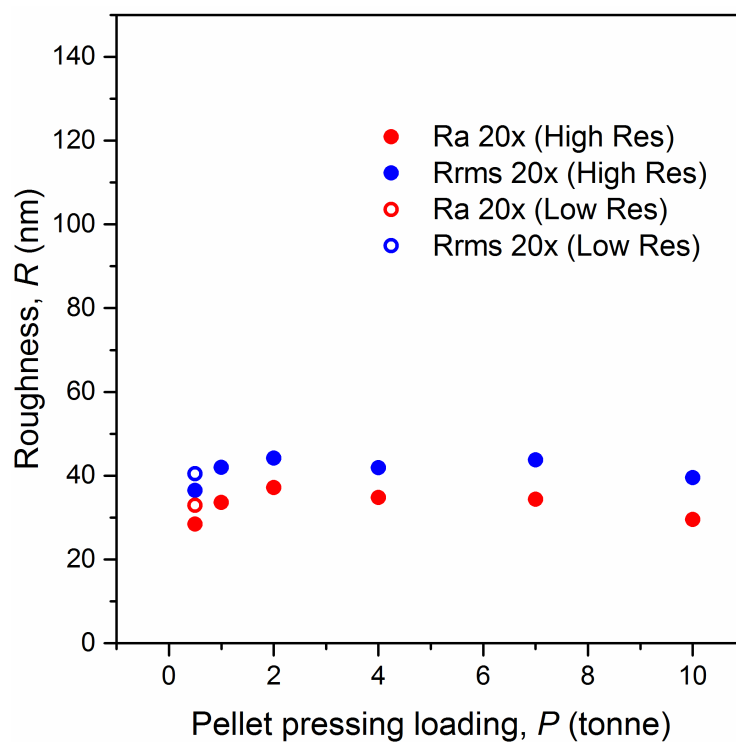


Fig. S11. Plot of the surface roughness against pelletization pressure for the ZIF-8 pellets. Measurements were performed using the Alicona InfiniteFocus 3D profilometer.

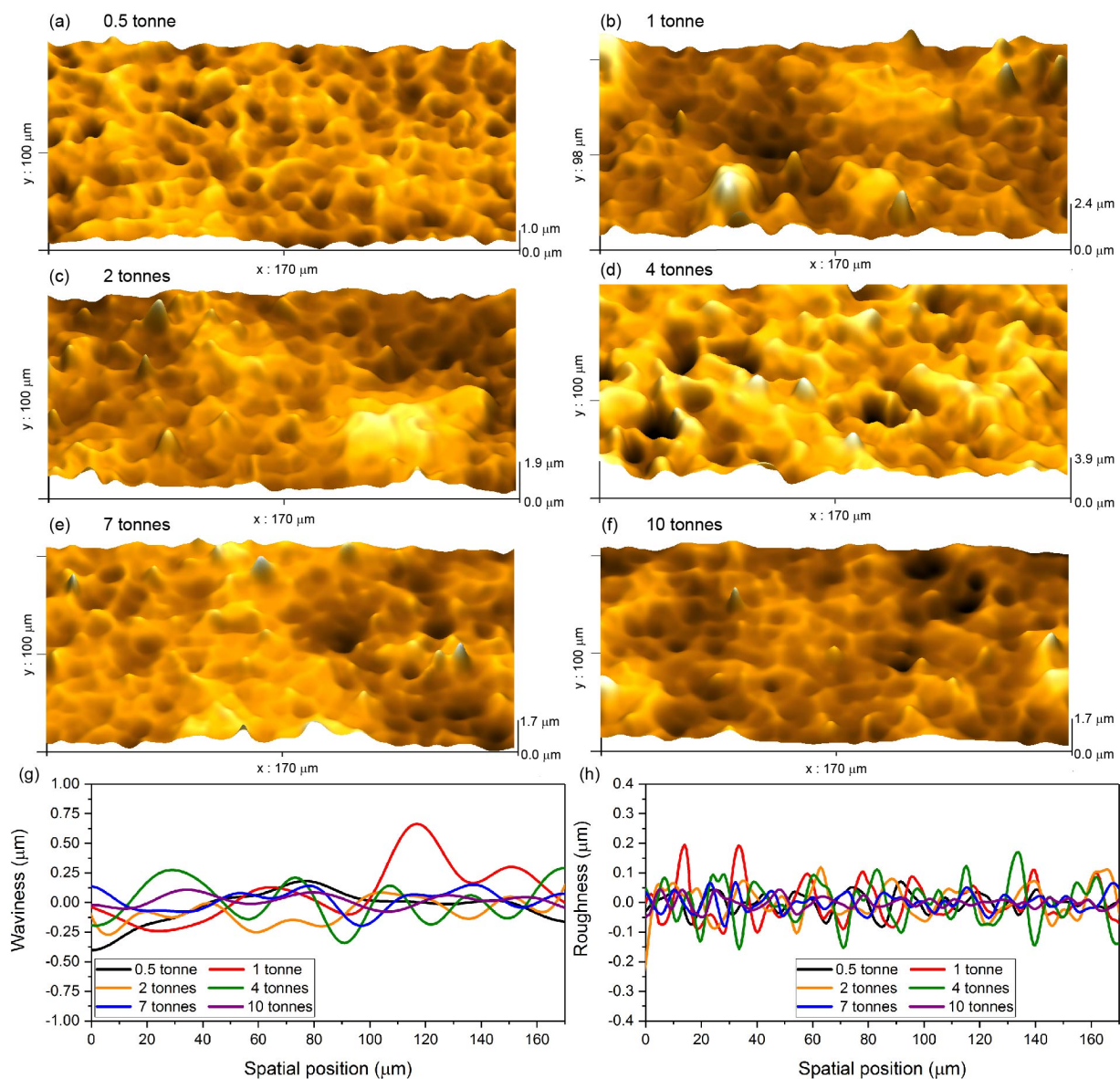


Fig. S12. Morphology of pellets pressed by different loads to evaluate surface roughness. Reconstructed 3D surface profiles (using Alicona InfiniteFocus, 50x objective magnification equipped with 20 nm vertical resolution) of pellets pressed under loads (a) 0.5 tonne, (b) 1 tonne, (c) 2 tonnes, (d) 4 tonnes, (e) 7 tonnes, (f) 10 tonnes; (g) Linear waviness and (h) roughness profile (the width of profile line is 80 μm) of pellets under various loads.

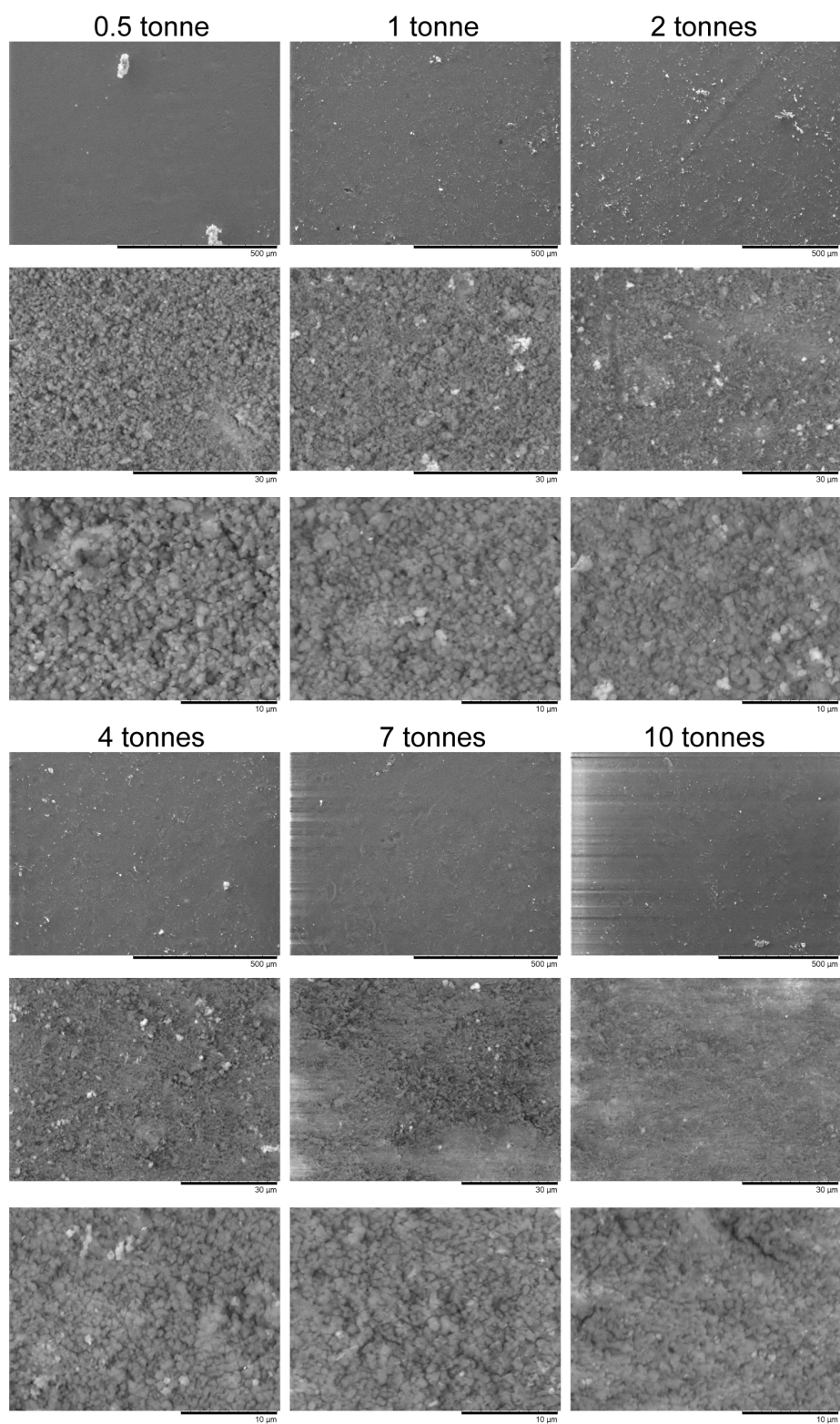


Fig. S13. Scanning electron microscope (SEM) images of the pellet surface of ZIF-8, compressed under 0.5-10 tonnes for a 13-mm diameter pellet (i.e. nominal pressure of 0.038-0.150 GPa). Three levels of magnifications are shown under each applied load.

4 Reflectivity Spectra in the Far-IR and Mid-IR Regions

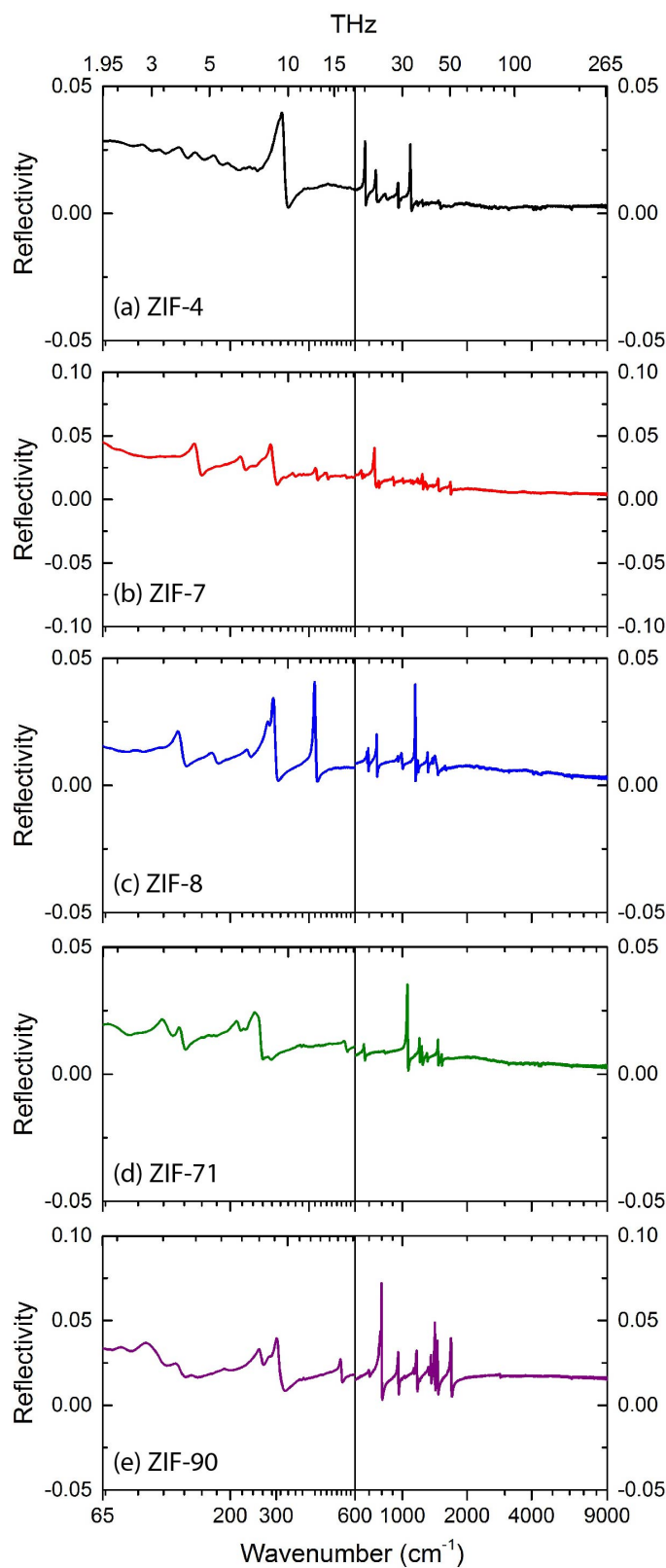


Fig. S14. Spectra of the far-IR and mid-IR spectral regions of (a) ZIF-4, (b) ZIF-7, (c) ZIF-8, (d) ZIF-71 and (e) ZIF-90. The spectra show the raw reflectivity data. The far-IR and mid-IR regions are both plotted on separate logarithmic axes for additional clarity.

5 Real and Imaginary Parts of the Complex Dielectric Constant and Complex Refractive Index

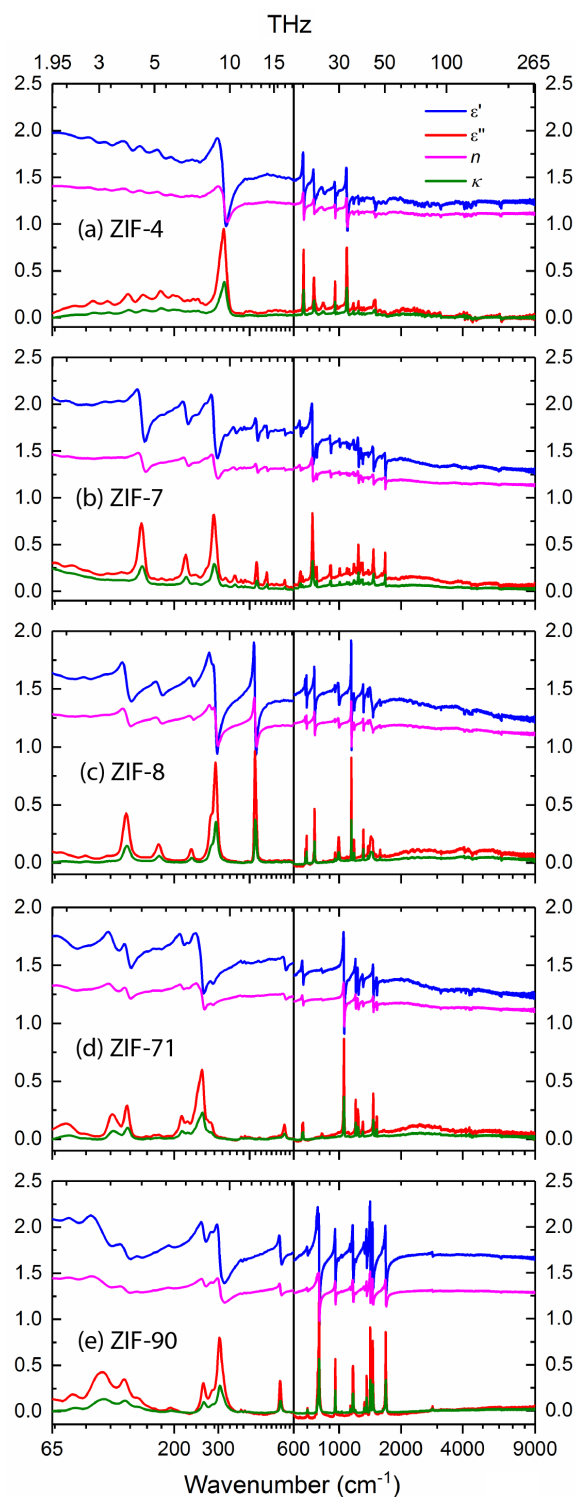


Fig. S15. Spectra of the far-IR and mid-IR spectral regions of (a) ZIF-4, (b) ZIF-7, (c) ZIF-8, (d) ZIF-71 and (e) ZIF-90. The spectra show the real (ϵ') and imaginary (ϵ'') parts of the dielectric function and the real (n) and imaginary (κ) parts of the refractive index. The far-IR and mid-IR regions are both plotted on separate logarithmic axes for additional clarity.

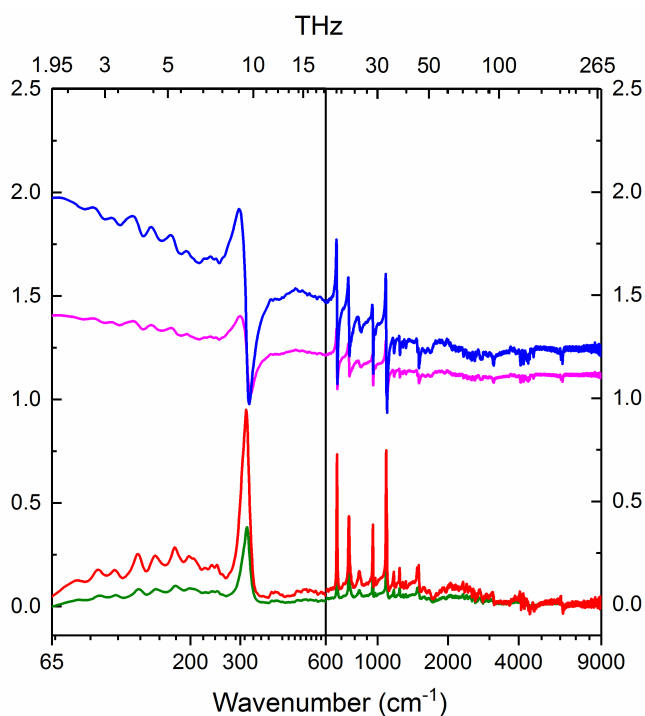


Fig. S16. Close up of the spectra in Fig. S15 of ZIF-4. The far-IR and mid-IR regions are both plotted on separate logarithmic axes for additional clarity. Colour code: Blue ϵ' , Red ϵ'' , Magenta n , Green κ .

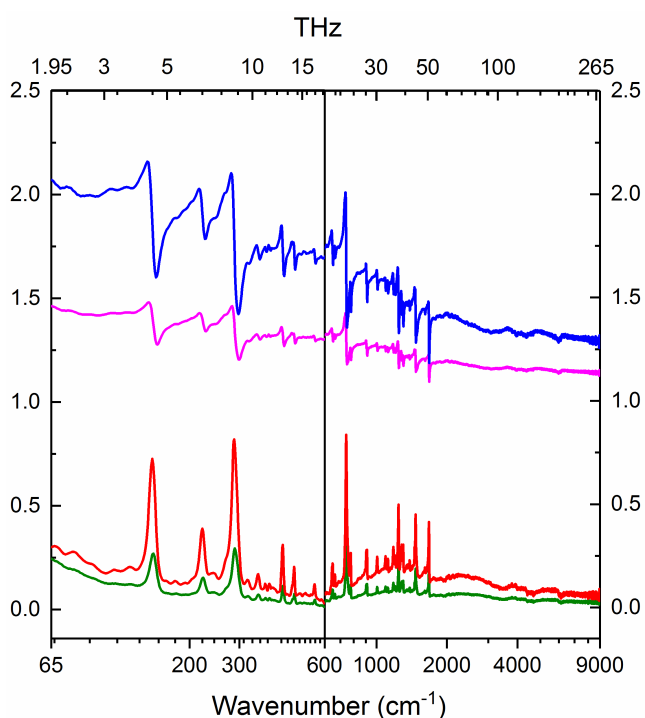


Fig. S17. Close up of the spectra in Fig. S15 of ZIF-7. The far-IR and mid-IR regions are both plotted on separate logarithmic axes for additional clarity. Colour code: Blue ϵ' , Red ϵ'' , Magenta n , Green κ .

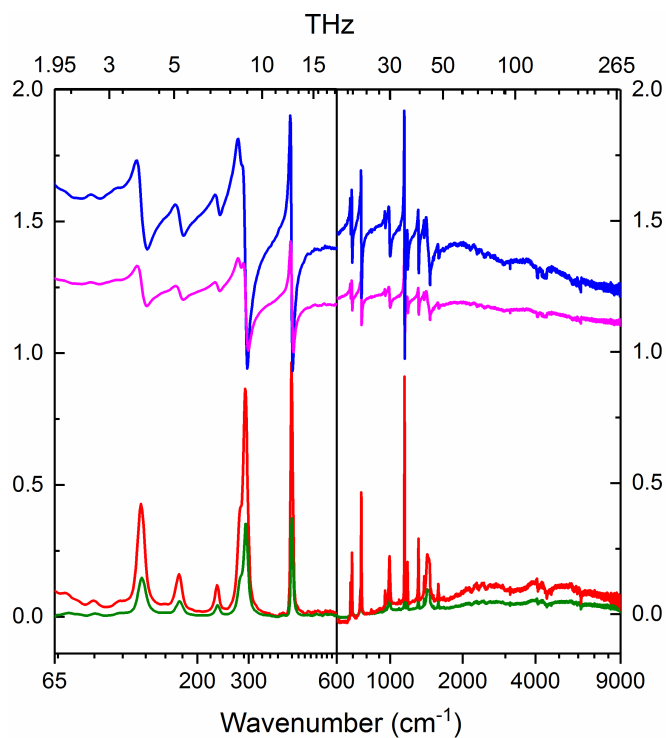


Fig. S18. Close up of the spectra in Fig. S15 of ZIF-8. The far-IR and mid-IR regions are both plotted on separate logarithmic axes for additional clarity. Colour code: Blue ϵ' , Red ϵ'' , Magenta n , Green κ .

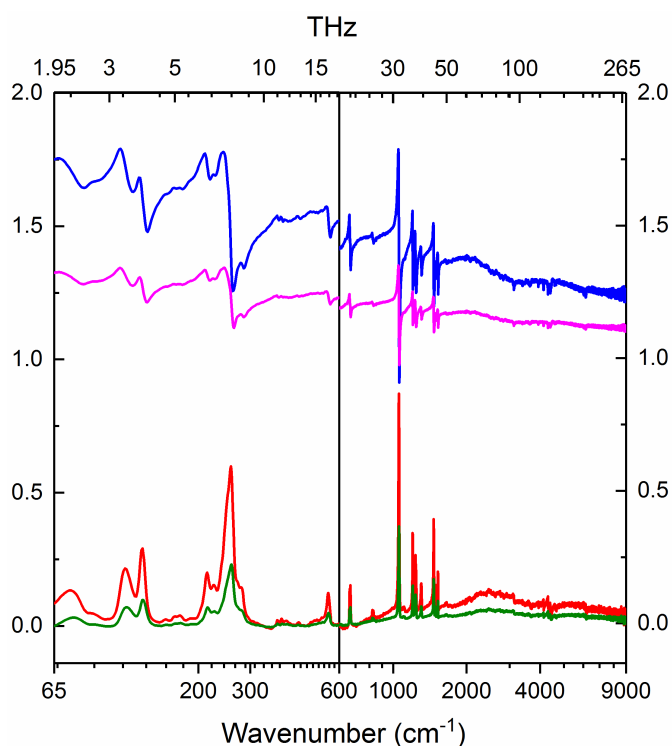


Fig. S19. Close up of the spectra in Fig. S15 of ZIF-71. The far-IR and mid-IR regions are both plotted on separate logarithmic axes for additional clarity. Colour code: Blue ϵ' , Red ϵ'' , Magenta n , Green κ .

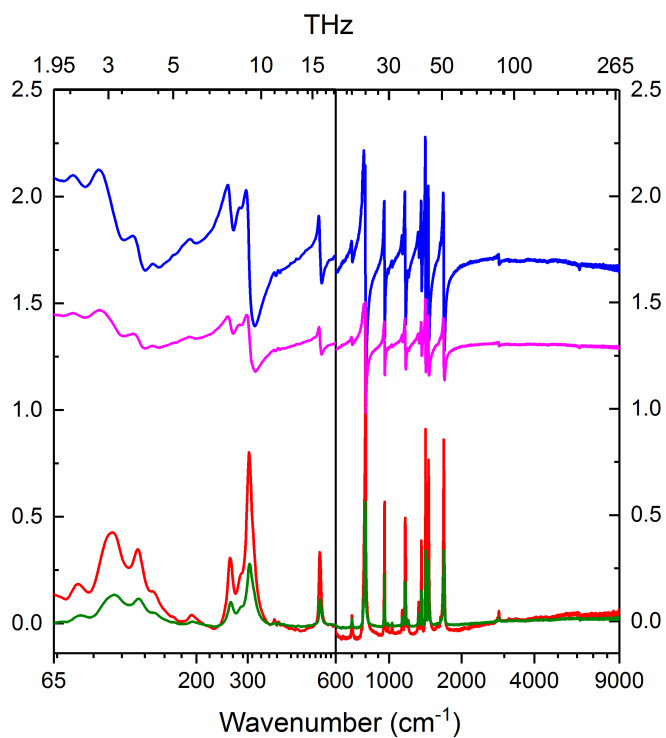


Fig. S20. Close up of the spectra in Fig. S15 of ZIF-90. The far-IR and mid-IR regions are both plotted on separate logarithmic axes for additional clarity. The disparity between the imaginary parts of the functions in the 600-2000 cm^{-1} spectral region is due to the KKT being performed over a selected limited range (see Section 7). Colour code: Blue ϵ' , Red ϵ'' , Magenta n , Green κ .

6 *Ab Initio* Density Functional Theory (DFT) Calculations

Density functional theory (DFT) calculations were performed at the B3LYP level of theory and corrected with an empirical dispersion term (B3LYP-D*).¹¹ The level of theory employed in our calculations is accurate enough for the purpose of our study*, as recently demonstrated in a series of MOF structures.¹² All of the calculations were performed with the periodic *ab initio* code CRYSTAL14.¹³ The code considers crystalline orbitals as linear combinations of Bloch functions (BF) and evaluates them using a regular three-dimensional (3D) mesh in the reciprocal space. Each BF was constructed from local atomic orbitals (AOs), which are linear combinations of Gaussian-type functions (GTF) and each GTF is the result of a Gaussian multiplied by a solid spherical harmonic. All electron TZVP basis sets were used for Zn, C, N, O, Cl, and H atoms.

The lattice parameters and atomic coordinates of the unit cell are both optimised at constant symmetry (maintaining the symmetry space group) *via* a normalized combined set of symmetrized directions and deformations using the CRYSTAL14 code.¹³ The optimization procedure was achieved by obtaining a gradient of the total energies of each optimization step. A Hessian matrix (matrix of second derivatives) was constructed from the energy gradients, and a quasi-Newtonian optimization algorithm was implemented in which a quadratic step (BFGS Hessian updating scheme) is combined with a linear parabolic fit.^{14,15,16,17,18} An optimised structure is defined by locating a minimum on the potential energy surface and this is assumed when the forces acting on the atoms in the unit cell are numerically zero. The optimization procedure defines this as the point where the root mean square (RMS) and the absolute value of the largest component of the gradients and the estimated displacements are below a defined threshold. The threshold for the maximum and RMS gradient, and the maximum and RMS atomic displacement of all atoms was set to 1.5×10^{-4} , 1.0×10^{-4} , 3.0×10^{-4} and 2.0×10^{-4} a.u., respectively for all optimizations. The optimization was considered to have completed when all four conditions were simultaneously satisfied. In addition, the self-consistent field (SCF) convergence threshold was also improved from 10^{-7} a.u. to 10^{-10} a.u on the total energy and tighter tolerances for the evaluation of two-electron integrals were used.

The harmonic vibrational frequencies were calculated from a mass-weighted Hessian matrix, obtained by numerical differentiation of the analytical first derivatives (gradients). The total energies for the gradients were calculated from geometries obtained by slightly displacing, in turn, each of the $3N$ nuclear coordinates with respect to the equilibrium geometry. The symmetry is maintained at each geometry and the second derivatives are performed only on the asymmetric unit cell (the irreducible atoms). The Hessian matrix is then constructed using the point group symmetry and diagonalized to obtain the eigenvalues and eigenvectors, resulting in the vibrational frequencies (cm^{-1}) and normal modes respectively. The IR intensities are obtained from the CPHF (or CPKS) approach.¹⁹

Eckart conditions are imposed on the Hessian matrix to reduce numerical noise. This is achieved *via* an automated process to isolate the purely translational and rotational degree of freedom in the system. The vibrational frequencies are the modes located at the Γ -point, as the volume of each system studied is sufficiently large to expect negligible phonon dispersion.

The static dielectric constants were calculated analytically *via* a Coupled-Perturbed Hartree-Fock / Kohn-Sham (CPHF/CPKS) approach.^{20,21} The CPHF/CPKS method involves computing the polarizability (or dielectric) tensor and optionally the first and second order hyper-polarizability. However, for the work in this letter, the total energy of the material in a constant static field was calculated from the following equation, truncated at the second order, therefore not including the contributions from the hyper-polarizabilities:

$$E(\boldsymbol{\varepsilon}) = E(0) - \sum_t \mu_t \varepsilon_t - \frac{1}{2} \sum_{tu} \alpha_{tu} \varepsilon_t \varepsilon_u - \dots$$

Where $E(0)$ is the field-free energy, $\boldsymbol{\varepsilon}$ is the electric field, $\boldsymbol{\mu}$ is the dipole moment and $\boldsymbol{\alpha}$ is the polarizability. The dipole moment and the polarizability are related to the energy derivatives according to the following equations, although a much more in depth explanation can be found in Ref.22:

$$\mu_t = -\frac{\partial E}{\partial \varepsilon_t}$$

$$\alpha_{iu} = -\frac{\partial^2 E}{\partial \varepsilon_i \partial \varepsilon_u}$$

The frequency-dependent (dynamic) reflectance spectra and dielectric constant, were calculated via combining the frequency-independent optical dielectric tensor with the vibrational frequencies. The complex dielectric tensor is calculated for each unique direction of polarization via a classical Drude-Lorentz model:

$$\varepsilon_{a,b,c}(\nu) = \varepsilon_{\infty,a,b,c} + \sum_p \frac{f_{p,a,b,c} \nu_p^2}{\nu_p^2 - \nu^2 - i\nu\gamma_p}$$

Where a, b, c indicates the polarization direction in the crystal, ε_{∞} is the static dielectric tensor, ν_p is the TO frequency, f_p is the oscillator strength and γ_p is a damping factor for the p^{th} vibrational mode (set to 5.0 cm^{-1} in the calculations). The reflectance curve is then calculated for each unique direction from the equation below:

$$R_{ii}(\nu) = \left| \frac{\sqrt{\varepsilon_{a,b,c}(\nu) - \sin^2(\theta)} - \cos(\theta)}{\sqrt{\varepsilon_{a,b,c}(\nu) - \sin^2(\theta)} + \cos(\theta)} \right|^2$$

Where θ is the angle of incidence and was set to 30° in the calculation to match with the experimental spectra. For example, the dynamic dielectric spectrum reported for ZIF-8 is independent of the crystallographic direction, as the structure is cubic ($a = b = c$).

Note that although GW and GW+BSE methods have been shown to achieve accurate band structure and response properties of solids, but despite the recent developments towards applications to large systems (e.g. ref.23) it is still prohibitively computationally demanding for application to complex systems such as MOFs. In this respect, hybrid functionals such as B3LYP-D adopted in the present work, represent a computationally more affordable alternative and a practical way to obtain accurate results in many cases comparable to GW.²⁴

7 ZIF-8 Spectral Features and Correction

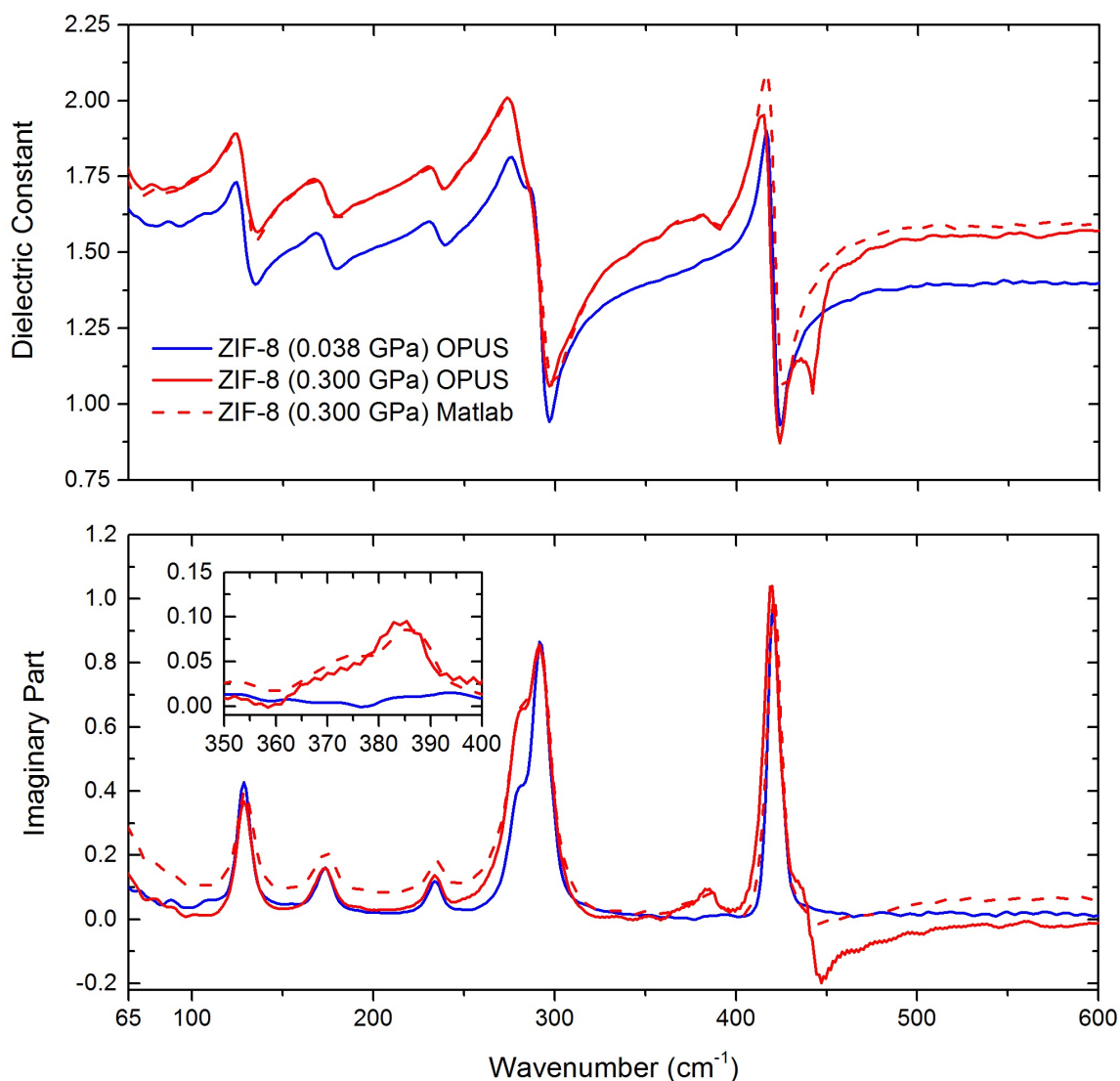


Fig. S21. Plots of the real and imaginary parts of the dielectric function from the KKT of ZIF-8 showing the evolution of a new absorption feature at $\sim 385 \text{ cm}^{-1}$ upon a pelletization pressure above 0.300 GPa. An artefact is also introduced at $\sim 450 \text{ cm}^{-1}$ and is the result of the KKT being performed over a selected spectral range instead of zero to infinity. This can be eliminated by extrapolation and shows any artificial negative values disappear using a customised Matlab code implemented in ref.25.

8 References

- (1) Bennett, T. D.; Goodwin, A. L.; Dove, M. T.; Keen, D. A.; Tucker, M. G.; Barney, E. R.; Soper, A. K.; Bithell, E. G.; Tan, J. C.; Cheetham, A. K. Structure and properties of an amorphous metal-organic framework. *Phys. Rev. Lett.* **2010**, *104*, 115503.
- (2) Ryder, M. R.; Bennett, T. D.; Kelley, C. S.; Frogley, M. D.; Cinque, G.; Tan, J. C. Tracking thermal-induced amorphization of a zeolitic imidazolate framework via synchrotron in situ far-infrared spectroscopy. *Chem. Commun.* **2017**, *53*, 7041-7044.
- (3) Li, Y. S.; Liang, F. Y.; Bux, H.; Feldhoff, A.; Yang, W. S.; Caro, J. Molecular sieve membrane: Supported metal-organic framework with high hydrogen selectivity. *Angew. Chem. Int. Ed.* **2010**, *49*, 548-551.
- (4) Lively, R. P.; Dose, M. E.; Thompson, J. A.; McCool, B. A.; Chance, R. R.; Koros, W. J. Ethanol and water adsorption in methanol-derived ZIF-71. *Chem. Commun.* **2011**, *47*, 8667-8669.
- (5) Hua, D.; Ong, Y. K.; Wang, Y.; Yang, T.; Chung, T.-S. ZIF-90/P84 mixed matrix membranes for pervaporation dehydration of isopropanol. *J. Membr. Sci.* **2014**, *453*, 155-167.
- (6) Phan, A.; Doonan, C. J.; Uribe-Romo, F. J.; Knobler, C. B.; O'Keeffe, M.; Yaghi, O. M. Synthesis, structure and carbon dioxide capture properties of zeolitic imidazolate frameworks. *Acc. Chem. Res.* **2010**, *43*, 58-67.
- (7) Zhao, P.; Lampronti, G. I.; Lloyd, G. O.; Wharmby, M. T.; Facq, S.; Cheetham, A. K.; Redfern, S. A. T. Phase transitions in zeolitic imidazolate framework 7: The importance of framework flexibility and guest-induced instability. *Chem. Mater.* **2014**, *26*, 1767-1769.
- (8) Pike-Technologies. *Installation and user guide - VeeMAX II variable angle specular reflectance accessory*. PIKE Technologies, Inc.: Madison, U.S.A.; **2012**.
- (9) Lucarini, V.; Saarinen, J. J.; Peiponen, K. E.; Vartiainen, E. M. *Kramers-Kronig relations in optical materials research*. Springer-Verlag: Berlin Heidelberg; **2005**.
- (10) Bruker. *OPUS spectroscopy software (version 7)*, **2017**, <https://www.bruker.com/products/infrared-near-infrared-and-raman-spectroscopy/opus-spectroscopy-software.html>
- (11) Civalleri, B.; Zicovich-Wilson, C. M.; Valenzano, L.; Ugliengo, P. B3LYP augmented with an empirical dispersion term (B3LYP-D*) as applied to molecular crystals. *CrystEngComm* **2008**, *10*, 405-410.
- (12) Ryder, M. R.; Donà, L.; Vitillo, J. G.; Civalleri, B. Understanding and controlling the dielectric response of metal-organic frameworks. *ChemPlusChem* **2018**, (In Press, DOI: 10.1002/cplu.201700558).
- (13) Dovesi, R.; Orlando, R.; Erba, A.; Zicovich-Wilson, C. M.; Civalleri, B.; Casassa, S.; Maschio, L.; Ferrabone, M.; De La Pierre, M.; D'Arco, P., et al. CRYSTAL14: A program for the *ab initio* investigation of crystalline solids. *Int. J. Quantum Chem.* **2014**, *114*, 1287-1317.
- (14) Broyden, C. G. The convergence of a class of double-rank minimization algorithms: 2. The new algorithm. *IMA J. Appl. Math.* **1970**, *6*, 222-231.
- (15) Broyden, C. G. The convergence of a class of double-rank minimization algorithms 1. General considerations. *IMA J. Appl. Math.* **1970**, *6*, 76-90.

- (16) Fletcher, R. A new approach to variable metric algorithms. *Comput. J.* **1970**, *13*, 317-322.
- (17) Goldfarb, D. A family of variable-metric methods derived by variational means. *Math. Comput.* **1970**, *24*, 23-26.
- (18) Shanno, D. F. Conditioning of quasi-newton methods for function minimization. *Math. Comput.* **1970**, *24*, 647-656.
- (19) Maschio, L.; Kirtman, B.; Orlando, R.; Rerat, M. Ab initio analytical infrared intensities for periodic systems through a coupled perturbed Hartree-Fock/Kohn-Sham method. *J. Chem. Phys.* **2012**, *137*.
- (20) Maschio, L.; Kirtman, B.; Rerat, M.; Orlando, R.; Dovesi, R. Ab initio analytical raman intensities for periodic systems through a coupled perturbed Hartree-Fock/Kohn-Sham method in an atomic orbital basis. I. Theory. *J. Chem. Phys.* **2013**, *139*, 164101.
- (21) Maschio, L.; Kirtman, B.; Rerat, M.; Orlando, R.; Dovesi, R. Ab initio analytical raman intensities for periodic systems through a coupled perturbed Hartree-Fock/Kohn-Sham method in an atomic orbital basis. II. Validation and comparison with experiments. *J. Chem. Phys.* **2013**, *139*, 164102.
- (22) Ferrero, M.; Rerat, M.; Orlando, R.; Dovesi, R. The calculation of static polarizabilities of 1-3D periodic compounds. The implementation in the CRYSTAL code. *J. Comput. Chem.* **2008**, *29*, 1450-1459.
- (23) Govoni, M.; Galli, G. Large scale GW calculations. *J. Chem. Theory Comput.* **2015**, *11*, 2680-2696.
- (24) Gerosa, M.; Bottani, C. E.; Di Valentin, C.; Onida, G.; Pacchioni, G. Accuracy of dielectric-dependent hybrid functionals in the prediction of optoelectronic properties of metal oxide semiconductors: A comprehensive comparison with many-body GW and experiments. *J. Phys.: Condens. Matter.* **2018**, *30*, 044003.
- (25) Titov, K.; Zeng, Z.; Ryder, M. R.; Chaudhari, A. K.; Civalleri, B.; Kelley, C. S.; Frogley, M. D.; Cinque, G.; Tan, J. C. Probing dielectric properties of metal-organic frameworks: MIL-53(Al) as a model system for theoretical predictions and experimental measurements via synchrotron far- and mid-infrared spectroscopy. *J. Phys. Chem. Lett.* **2017**, *8*, 5035-5040.